UNIVERSITÉ DE GENÈVE

Archive ouverte UNIGE
https://archive-ouverte.unige.ch

Article scientifique | Article | 2013

Published version | Open Access

This is the published version of the publication, made available in accordance with the publisher's policy.

Age-dependent small-animal internal radiation dosimetry

Xie, Tianwu; Zaidi, Habib

How to cite

XIE, Tianwu, ZAIDI, Habib. Age-dependent small-animal internal radiation dosimetry. In: Molecular imaging, 2013, vol. 12, n° 6, p. 364–375.

This publication URL: https://archive-ouverte.unige.ch/unige:40167

© This document is protected by copyright. Please refer to copyright holder(s) for terms of use.

RESEARCH ARTICLE

Age-Dependent Small-Animal Internal Radiation Dosimetry

Tianwu Xie and Habib Zaidi

Abstract

Rats at various ages were observed to present with different radiosensitivity and bioavailability for radiotracers commonly used in preclinical research. We evaluated the effect of age-induced changes in body weight on radiation dose calculations. A series of rat models at different age periods were constructed based on the realistic four-dimensional digital rat whole-body (ROBY) computational model. Particle transport was simulated using the *MCNPX* Monte Carlo code. Absorbed fractions (AFs) and specific absorbed fraction (SAFs) of monoenergetic photons/electrons and S values of eight positron-emitting radionuclides were calculated. The SAFs and S values for most source-target pairs were inversely correlated with body weight. Differences between F-18 S values for most source-target pairs were between −1.5% and −2%/10 g difference in body weight for different computational models. For specific radiotracers, the radiation dose to organs presents a negative correlation with rat body weight. The SAFs for monoenergetic photons/electrons and S values for common positron-emitting radionuclides can be exploited in the assessment of radiation dose delivered to rats at different ages and weights. The absorbed dose to organs is significantly higher in the low-weight young rat model than in the adult model, which would result in steep secondary effects and might be a noteworthy issue in laboratory animal internal dosimetry.

THE RAT AS A MODEL of human disease is prized as a preeminent laboratory animal in biomedical research owing to the various advantages it offers in translational animal research. This includes the fact that the rodent genome is similar to the human genome and a large number of rodents can be reared in a short time; moreover, the breeding of rats in the laboratory is easy and less costly. At the beginning of the twentieth century, The Wistar Institute developed the first notable rat strain as a model organism for biological and medical research.[1] The Wistar rat is one of the most popular rat strains used for laboratory research, and more than half of currently used laboratory rat strains are descendents from the original colony established by this institute.[2] They are widely used in preclinical trials for tracer development, test of novel medical imaging methods, and many other biomedical research areas.[3–5] Clear pictures of disease in small animals can be obtained using dedicated high-resolution preclinical positron emission tomography (PET) instrumentation, which enables researchers to track molecular events in vivo and probe the biological basis of human disease. However, in typical preclinical PET–computed tomography (CT) imaging studies, the animal is often exposed to nonnegligible radiation exposure, which may preclude the use of the animal in longitudinal studies, where it is used as its own control. In this context, the accurate assessment of radiation dose delivered to laboratory animals in experiments involving the use of stand-alone or hybrid imaging techniques (eg, PET, PET-CT) is of paramount importance.

For this purpose, various computational models have been developed to mimic the morphology and internal anatomic structures of small animals and used to assess the radiation dose delivered to laboratory animals in preclinical research studies. Hui and colleagues developed the first computational mouse model using simple equation-based mathematical functions to represent internal organs.[6] Further improvement led to finer mathematical small-animal models containing more internal organs and even realistic tumor models.[7–11] With the popularity and widespread availability of Monte Carlo–based radiation transport packages and the growth of high-performance computing, including cloud computing, voxel-based small-animal models of different specimens employing voxel matrices derived from tomographic images, which best preserve anatomic authenticity,

From the Division of Nuclear Medicine and Molecular Imaging, Geneva University Hospital, and the Geneva Neuroscience Center, Geneva University, Geneva, Switzerland, and the Department of Nuclear Medicine and Molecular Imaging, University of Groningen, University Medical Center Groningen, Groningen, the Netherlands.

Address reprint requests to: Habib Zaidi, PhD, Division of Nuclear Medicine and Molecular Imaging, Geneva University Hospital, CH-1211 Geneva, Switzerland; e-mail: habib.zaidi@hcuge.ch.

DOI 10.2310/7290.2013.00053

© *2013 Decker Publishing*

DECKER

have been developed for imaging and radiation dosimetry applications.[12–21] However, there is an intrinsic variability in organ mass and total body weight between these computational models owing to individual differences between studies specimens. Moreover, the body weight and length of laboratory animals used in longitudinal studies vary according to age periods. The rat at different ages can be linked to human beings in various growth phases[22–24] and was observed to have different radiosensitivity and bioavailability for radiotracers.[25–30] However, the intrinsic disadvantages of traditional mathematical and voxel-based models, such as the loss of most anatomic details and the difficulty in reshaping the contours of organs, obstructed the progress of radiation dosimetry research for small animals at different age periods. More recently, nonuniform rational B-spline surfaces (NURBS)-based modeling techniques have become popular for Monte Carlo–based radiation transport calculations.[21,31,32] The NURBS-based model holds most anatomic characteristics of internal organs and tissues and offers the flexibility of deforming these structures more realistically. As such, it became a precious tool for the assessment of age-dependent small-animal radiation dosimetry.

In this work, we used the four-dimensional digital rat whole-body (ROBY) NURBS-based Wistar rat model to produce a series of models representing the laboratory rat at 10 different age periods ranging between 4 weeks (prepubescent period) and 45 weeks (adult phase). For the adult rat older than 300 days, weight growth was reported to be due mostly to fat deposition.[33] Monte Carlo–based particle transport simulations of monoenergy photons/electrons and spectra corresponding to decay schemes of positron-emitting radionuclides (C-11, N-13, O-15, F-18, Cu-64, Ga-68, Y-86, and I-124) were performed using *MCNPX* (Los Alamos National Laboratory, Los Alamos, NM) to calculate the absorbed fractions (AFs), specific absorbed fractions (SAFs), and S values for the considered series of models. The obtained radiation dosimetry database can be used for the assessment of radiation dose to small animals in experiments involving the use of specimens at different age periods. Understanding the variability of the absorbed dose with body weight is important to appreciate the uncertainties involved in small-animal internal radiation dosimetry calculations.

Materials and Methods

Design of Computational Rat Models

Given that the Wistar rat is one of the most popular rat strains used in small-animal research, we constructed a series of anatomic models using the realistic ROBY model[31] derived from magnetic resonance images of a Wistar specimen according to published weight and length values for this strain. The growth chart was obtained from 2-year study data on the Wistar Hannover GALAS rat[34] and used to calculate the length of rats at different age periods based on the weight-length formulas (no gender distinction) given by Donaldson[35]:

$$\text{Body length} = 143 \times \log(\text{Body weight} + 15) - 134 \qquad (1)$$

The body weight and length values summarized in Table 1 were used as the basis for modification of the original ROBY model. The models representing 4-, 6-, 8-, 10-, 12-, 15-, 21-, 27-, 35-, and 45-week-old Wistar rats were constructed and referred to as rat models 1 to 10, respectively. The resulting organ masses were also adjusted to follow reference data reported in the literature.[35] The resulting organ and body masses were calculated by multiplying each organ volume by its corresponding density. Traditional hollow organs (eg, heart, stomach, intestines, and bladder) were treated as uniform organs, with mass corresponding to the sum of wall and content. The skeleton was treated as a mixture of 70% bone, 25% red bone marrow, and 5% yellow bone marrow.[36] Table 2 summarizes the body size (lateral size, anteroposterior size, and length), model weight, and calculated mass for each organ of the constructed anatomic models. Figure 1 shows ventral-dorsal views of representative rat models.

Monte Carlo Simulations

The modified NURBS-based rat models were voxelized using the ROBY software[31] and used as input to *MCNPX*

Table 1. Growth Chart and Length for the Wistar Rat at Different Ages

Model	*Age (wk)*	*Weight* (g)*	*Length† (mm)*
1	4	88	154
2	6	132	176
3	8	217	204
4	10	275	218
5	12	314	226
6	15	352	233
7	21	399	240
8	27	438	246
9	35	471	250
10	45	509	255

*The growth chart was obtained from 2-year study data on the Wistar Hannover GALAS rat.[34]

†The length was calculated according to the weight-length formula given by Donaldson.[35]

Table 2. Summary of Organ Masses and Body Sizes of the 10 Computational Rat Models at Different Ages

	Rat Model									
	1	*2*	*3*	*4*	*5*	*6*	*7*	*8*	*9*	*10*
Age (wk)	4	6	8	10	12	15	21	27	35	45
Mass (g)										
Other tissues	57.09	87.19	146.61	187.16	214.16	241.98	275.17	302.26	326.20	353.66
Skeleton	9.27	13.52	21.54	26.85	30.35	33.86	38.11	41.55	44.48	47.90
Heart	0.60	0.90	1.48	1.87	2.13	2.40	2.72	2.98	3.21	3.47
Lung	0.31	0.45	0.73	0.92	1.05	1.16	1.32	1.44	1.55	1.67
Liver	2.72	4.14	6.94	8.85	10.13	11.42	12.98	14.25	15.38	16.67
Stomach	1.19	1.80	3.02	3.85	4.40	4.96	5.63	6.19	6.67	7.22
Kidney	0.53	0.82	1.36	1.74	2.00	2.24	2.56	2.81	3.04	3.28
Intestines	6.56	9.89	16.39	20.75	23.64	26.62	30.17	33.05	35.59	38.52
Spleen	0.25	0.36	0.59	0.73	0.83	0.92	1.03	1.14	1.21	1.34
Bladder	0.17	0.26	0.42	0.53	0.60	0.67	0.76	0.83	0.90	0.96
Testis	0.04	0.07	0.11	0.14	0.15	0.17	0.20	0.22	0.24	0.25
Skin	7.97	10.47	14.60	16.94	18.40	19.86	21.50	22.75	23.88	25.05
Brain	1.33	1.99	3.30	4.19	4.78	5.39	6.11	6.70	7.22	7.81
Thyroid	0.07	0.11	0.18	0.22	0.25	0.28	0.32	0.35	0.37	0.41
Pancreas	0.13	0.21	0.34	0.43	0.49	0.56	0.63	0.69	0.74	0.81
Vas deferens	0.02	0.03	0.04	0.05	0.05	0.06	0.06	0.07	0.07	0.08
Total body	88.26	132.20	217.64	275.21	313.41	352.57	399.27	437.28	470.75	509.09
Size (mm)										
Lateral	38.00	44.00	52.00	57.00	60.00	63.00	66.00	68.00	70.00	72.00
Anteroposterior	28.00	32.00	38.00	42.00	44.00	46.00	48.00	50.00	52.00	53.00
Length	153.50	176.23	204.14	218.08	225.84	232.55	240.31	245.98	250.64	254.25

Monte Carlo code version 2.5.c[37] to simulate the transport and interaction of photons, electrons, and positrons in the computational rat models. The number of voxels for each identified region was calculated and multiplied by the voxel volume ($0.5 \times 0.5 \times 0.5$ mm^3) and corresponding tissue density to yield the region mass. The density and chemical composition of each organ were assumed to be similar to those of human beings.[38,39]

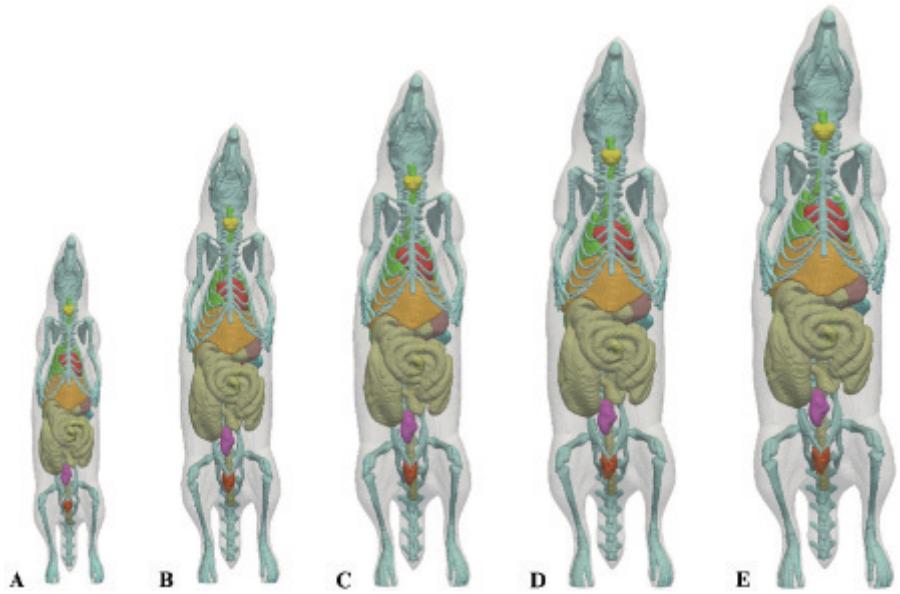

Figure 1. Three-dimensional visualization of representative computational rat models showing (A) the 4-, (B) 8-, (C) 12-, (D) 21-, and (E) 45-week-old models.

Uniformly distributed monoenergetic photon and electron sources, with 20 discrete photon energies ranging from 0.01 to 3.0 MeV and 13 selected electron energies ranging from 0.1 to 3.0 MeV, and eight positron-emitting sources (C-11, N-13, O-15, F-18, Cu-64, Ga-68, Y-86, and I-124) were simulated in 14 chosen source organs. A total of 6×10^6 primary particle histories were generated, resulting in a statistical uncertainty, in terms of coefficient of variation, of less than 2% in most cases. Ten parallel *MCNPX* simulation processes were run on a 12-core workstation with 2.4 GHz Intel Xeon processors and 32 GB RAM running Microsoft *Windows* 7 OS. The average calculation time corresponding to the number of particles reported for each simulation process is 156 minutes. The decay data of the positron-emitting radionuclides were taken from the Health Physics Society electronic resource.[40]

Absorbed Dose Calculation

The equation for mean absorbed dose calculation according to the Medical Internal Radiation Dose (MIRD) formalism is given by[41,42]

$$D(r_T,T_D) = \sum_{r_S} \int_0^{T_D} \widetilde{A}(r_S,t) S(r_T \leftarrow r_S)\, dt, \tag{2}$$

where $D(r_T,T_D)$ = the mean absorbed dose to a target region r_T over the dose integration period; T_D; $\widetilde{A}(r_S,t)$ = the time-dependent activity in source tissue r_S; and $S(r_T \leftarrow r_S)$ = the S value describing the equivalent dose rate to the target organ r_T per unit activity in the source organ r_S.

For certain radionuclides, the S value is given by

$$S(r_T \leftarrow r_S) = \frac{1}{M(r_T)} \sum_i E_i Y_i \phi(r_T \leftarrow r_S, E_i), \tag{3}$$

where E_i is the individual energy of the i^{th} nuclear transition, Y_i is number of i^{th} nuclear transitions per nuclear transformation, $M(r_T)$ is the mass of the target tissue r_T, and $\phi(r_T \leftarrow r_S, E_i)$ is the AF of radiation energy E_i in the target organ for the i^{th} radiation type originating in the source organ, which describes the proportion of energy released in source organs deposited in the target organ. The ratio of AF and target mass is known as the SAF, which describes the mean AF in the target organ.

If $\widetilde{A}(r_S,t)$ is normalized to a unit administered activity A_0, we obtain the mean absorbed dose per administered activity (absorbed dose coefficient):

$$\widetilde{D}(r_T,T_D) = \sum_{r_S} \int_0^{T_D} \frac{\widetilde{A}(r_S,t)}{A_0} S(r_T \leftarrow r_S)\, dt, \tag{4}$$

The fractional activity $\widetilde{A}(r_S,t)/A_0$ at a given time point of activity measurement is calculated by dividing the multiplicative combination of measured uptake (%ID/g) and the tissue weight by 100. The time–fractional activity curve (TAC) for considered source organs r_s is derived from graphs of the fractional activity $\widetilde{A}(r_S,t)/A_0$ versus time (in seconds). The data are fitted to two-component exponential curves[43] using the nonlinear regression method. The activity as a function of time is given by:

$$\widetilde{A}(r_S,t)/A_0 = C_1 e^{-k_1 t} + C_2 e^{-k_2 t}, \tag{5}$$

where C_1 and C_2 are coefficients and k_1 and k_2 are time constants.

Results

The AFs and SAFs for monoenergetic photons and electrons for 16 source organs irradiating 17 target organs were calculated. Supplemental Tables S1 to S15 (available online only) provide detailed photon and electron SAF results and S values of the eight positron-emitting radionuclides for the considered source-target pairs in selected rat models. Figure 2 shows photon self-absorbed fractions for the liver and the heart for the 10 generated rat models. Comparisons with the results of Xie and colleagues, Stabin and colleagues, and Peixoto and colleagues are also made.[8,12,18] A consistent trend can be observed for the different rat models. The self-absorbed fractions present a negative correlation with photon energy and a positive correlation with the rat model's weight because increasing photon energy facilitates the escape of recoil electrons and scattered photons from the source organ, whereas the increased weight is accompanied by a larger volume, which extends the distance of particle transport and causes more energy deposition in the source organ. Figure 3 shows photon and electron self-absorbed SAFs for the stomach and kidney. The self-absorbed SAFs decrease when the particle energy or the body weight increases; the latter outcome can be deduced from the definition of the SAF itself. In human internal radiation dosimetry, the electron cross-absorbed SAF for organs is commonly neglected[44] because the range of low-energy electrons is smaller than the dimension of most human organs.[45] However, given that the body dimension of rats is much smaller, it is necessary to evaluate the cross-absorbed

SAF in small-animal dosimetry calculation. Figure 4 illustrates photon and electron cross-absorbed SAFs for the intestine irradiating the stomach and kidney. The increasing curves of electron cross-absorbed SAFs in Figure 4, B and D, indicate that more electrons escape from the source organ and stop in surrounding tissues when energy increases. The difference between the shapes of self-absorbed (see Figure 3, A and C) and cross-absorbed (see Figure 4, A and C) photon SAF curves is more pronounced in the lower-energy portion. The rising portion of cross-absorbed photon SAF curves is linked to the increase in the energy deposition in target organs from particles escaping from source organs as the initial energy increases. Above a certain initial photon energy, more and more particles escape from the rat body, consequently causing the drop of photon cross-absorbed SAFs. Figure 5 shows the SAFs for the total body irradiating the skeleton, which expresses high radiosensitivity and is considered one of the most important dose-limiting tissues. As can be seen in Figure 5A, the skeletal cross-absorbed photon SAFs are 170 to 530% higher in the 4-week-old model and 24 to 47% higher in the 15-week-old model compared to the 45-week-old model. On the other hand, the skeletal cross-absorbed electron SAFs are about 450% higher in the 4-week-old model and 43% higher in the 15-week-old model than in the 45-week-old model. Figure 6 shows photon and electron SAF ratios between various rat models (from the 4-week-old model to the 35-week-old model) to the rat model 10 (45 weeks old) for the total body irradiating itself. It was observed that when the emitted energy increases, the absolute difference in photon self-absorbed SAFs of total body between various models starts initially with a rapid decrease followed by a steady portion in the energy range 0.05 to 1.2 MeV and finally drops gradually. For electron SAFs of the total body irradiating itself, the absolute difference between various models slightly decreases while increasing electron energy.

Figure 7 and Figure 8 show self-absorbed S values for the kidney, skeleton, heart, and lung and cross-absorbed S values of different source-target organ pairs for the constructed rat models and the eight considered positron-emitting radionuclides (C-11, N-13, O-15, F-18, Cu-64, Ga-68, Y-86, and I-124). For all positron-emitting radionuclides, the S values decrease, whereas the model weight increases. As can be seen in Figure 7, among the considered radionuclides, O-15 emits positrons with high energy and frequency and produces the highest self-absorbed S values in most organs. Interpreting the dosimetric results of cross-absorbed S values is more complicated than interpreting those of self-absorbed S values. Y-86 generates the highest cross-absorbed S values in most source-target organ pairs for different models, whereas Ga-68 induces the highest cross-absorbed S values in adjacent target organs for models with a lower weight. The relative differences in S values per 10 g difference in total body mass (%/10 g) for F-18 between the 4-week-old and 45-week-old models are summarized in Table 3. The relative difference ranges between −1.5% and −2%/10 g for most source-target pairs. Figure 9 shows the contributions of positrons and the two annihilation photons to the total body self-absorbed S values of C-11, N-13, O-15, and F-18 in the 10 rat models. It can be seen that for these four radionuclides, the larger contribution (more than 70%) to the self-absorbed S values is due to positron interactions, whereas the contribution of the two annihilation photons increases gradually with the weight.

We selected from the literature a ^{11}C-labeled probe used in small-animal PET imaging to evaluate the effect of age-induced changes in rat weight on absorbed dose and illustrate the application of the produced S values to the

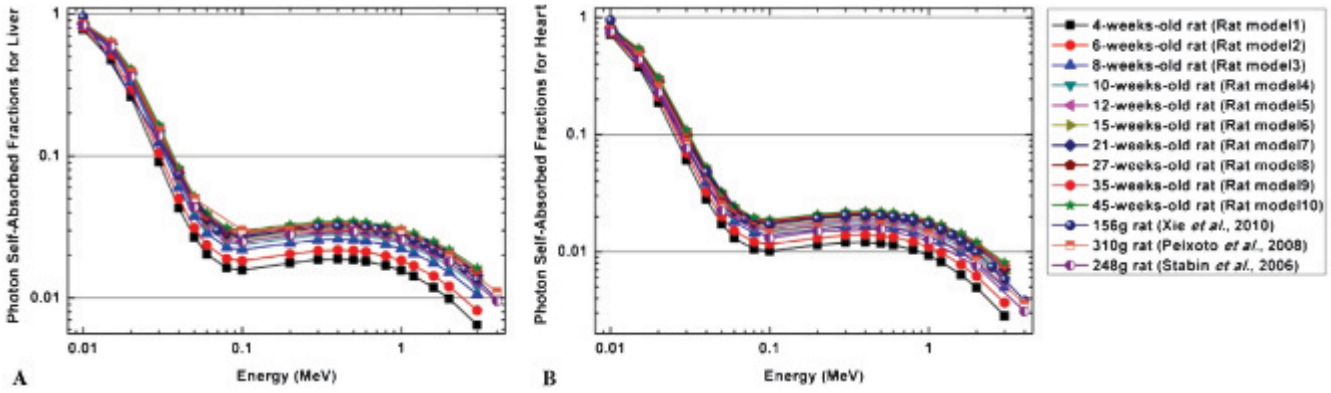

Figure 2. Photon self-absorbed fractions for (A) the liver and (B) the heart for computational rat models at different ages. A comparison with published results by Xie and colleagues, Stabin and colleagues, and Peixoto and colleagues is also shown.[8,12,18]

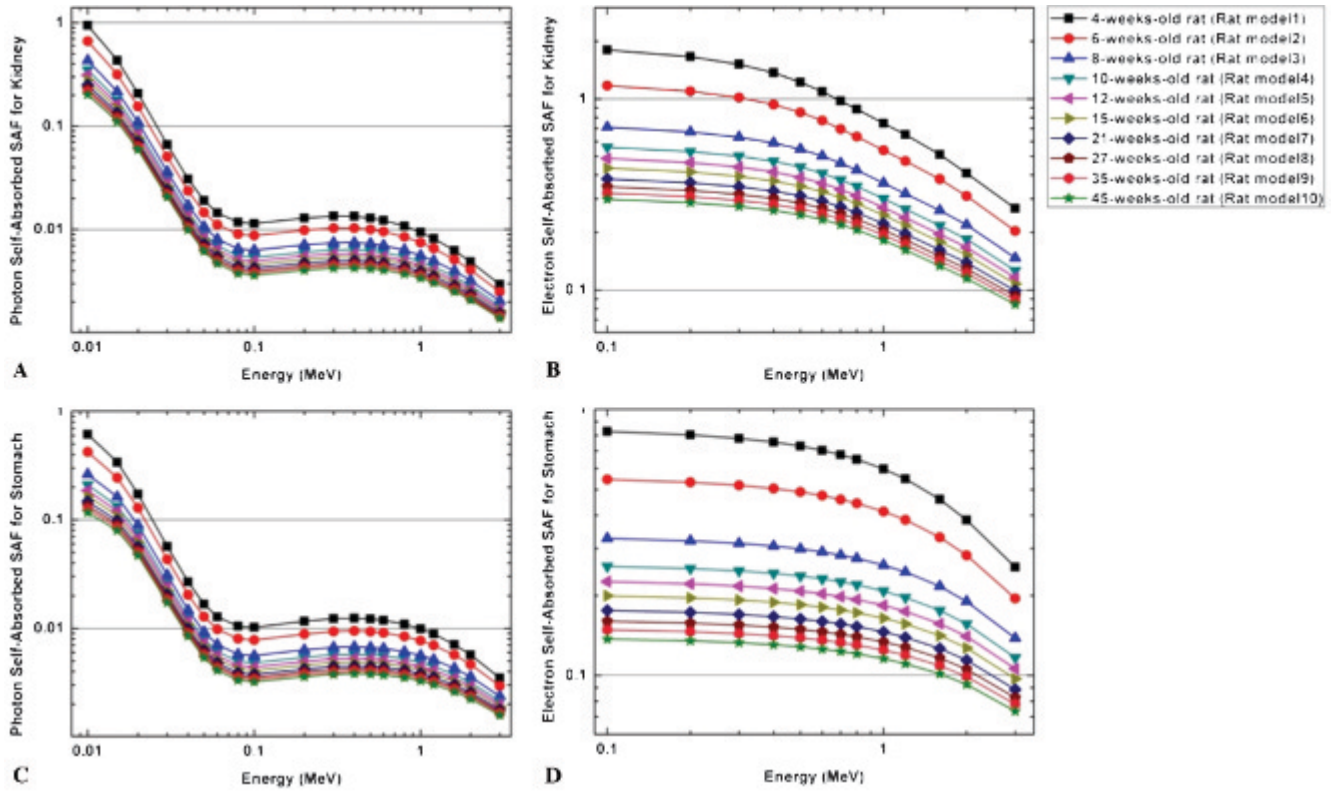

Figure 3. Photon self-absorbed specific absorbed fractions (SAFs) for (A) the stomach and (C) the kidney and electron self-absorbed SAFs for (B) the stomach and (D) the kidney.

assessment of the corresponding absorbed dose to small animals using the MIRD schema. ^{11}C-labeled 3-amino-4-(2-dimethylaminomethyl-phenylsulfanyl)-benzonitrilev (^{11}C-DASB) is a recently introduced probe for imaging serotonin transporters using PET.[46] According to the reported biodistribution data, internal organs are divided into two groups: organs with time-varying uptake given in Wilson and colleagues[46] (Figure 10A) and organs/tissues in the remaining body (Figure 10B), assuming a uniform uptake assigned according to the residual activity. The TACs of each organ were obtained by fitting the biodistribution data of ^{11}C-DASB in the rat according to equation 5 and used to calculate the absorbed dose to organs in the 10 rat models. The absorbed dose results are illustrated in Figure 10, where the comparisons are made between the different models.

Discussion

Monte Carlo techniques are widely used in small-animal radiation dose calculations, in which trustworthy evaluation of radiation dosimetry is grounded on reliable computational models. However, a discrepancy between a computational model and the real anatomy of laboratory specimen commonly occurs, especially when the inanimate computational model is used to mimic a living and growing laboratory animal. Given that laboratory animals have substantially different physical characteristics and present with significantly different radiosensitivity and bioavailability for various radiopharmaceuticals at different age periods, it is recommended to evaluate the age-dependent absorbed dose to small animals.

In this work, we constructed a series of rat models at 10 different age periods and used Monte Carlo calculations to compare the AFs and SAFs of monoenergy photons and electrons and the S values of commonly used positron-emitting radionuclides in various source-target pairs. The self-absorbed AFs are positively correlated with the age and the mass because enlarging the source region results in more energy deposition of particles. The SAFs for all source-target pairs decrease when increasing body mass. Further significant changes are more apparent at low-photon energies, which indicate that the contribution to radiation dose from low-energy photon emitters is more sensitive to the change in weight and may result in a significantly higher absorbed dose in the young rat.

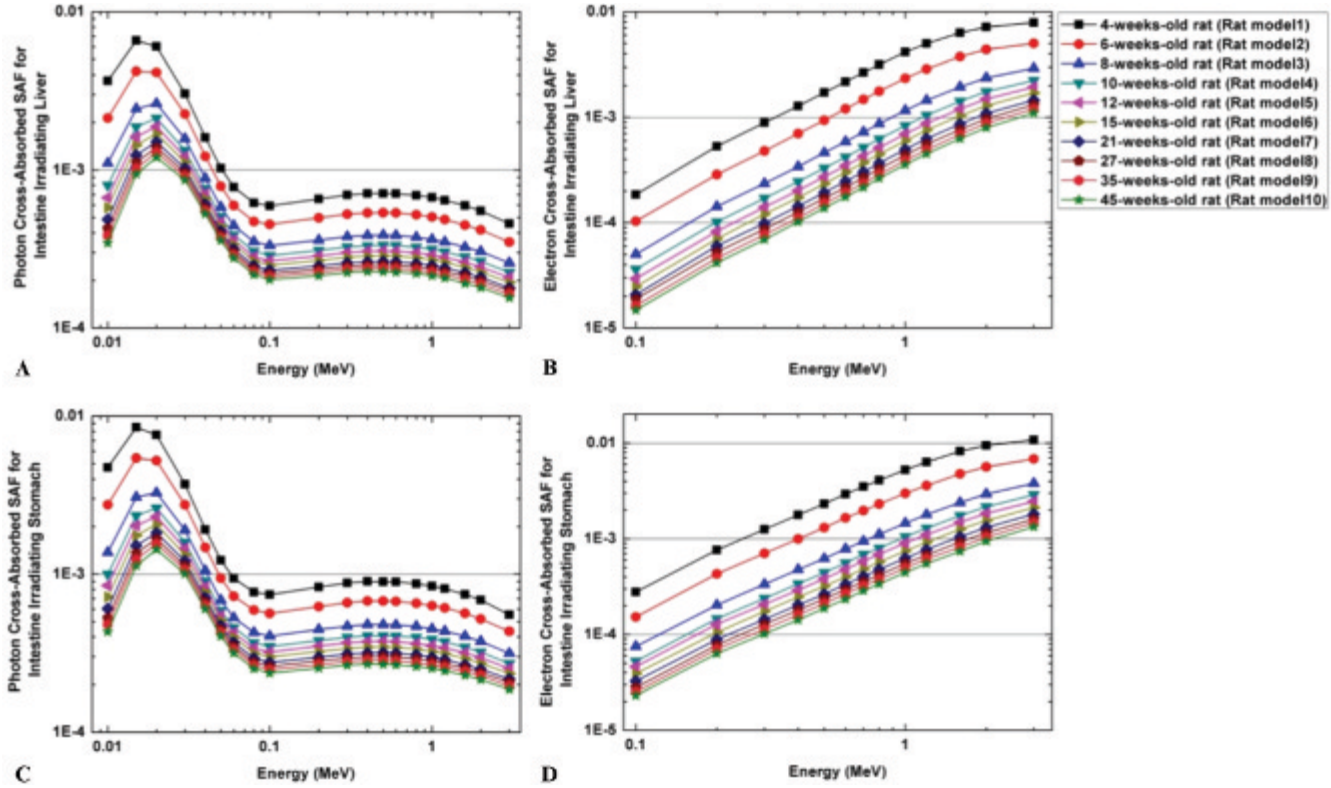

Figure 4. Photon cross-absorbed specific absorbed fractions (SAFs) for the intestine irradiating (A) the stomach and (C) the kidney and electron cross-absorbed SAFs for the intestine irradiating (B) the stomach and (D) the kidney.

Changes in S values with age and weight were also evaluated for eight positron-emitting radionuclides commonly used in PET molecular imaging–based research. For all source-target pairs, S values decrease when increasing the age and weight. The contribution from the two annihilation photons to the total S values of positron emitters in the whole body is positively correlated with the age-dependent body weight. These results suggest that the activity administered to small animals for PET imaging produces a higher equivalent dose rate in the young rat than in the adult rat. Moreover, given that some tissues of young animals have higher sensitivity to ionizing radiation, this might result in higher radiation risks.[30,47–49] Assessment of the internal radiation dose delivered to small animals in experimental research is important for determining the radiotoxicity and therapeutic effect of radiotracers. In this regard, assessment of the variability of S values with changes in weight at different ages is an important issue. Considering

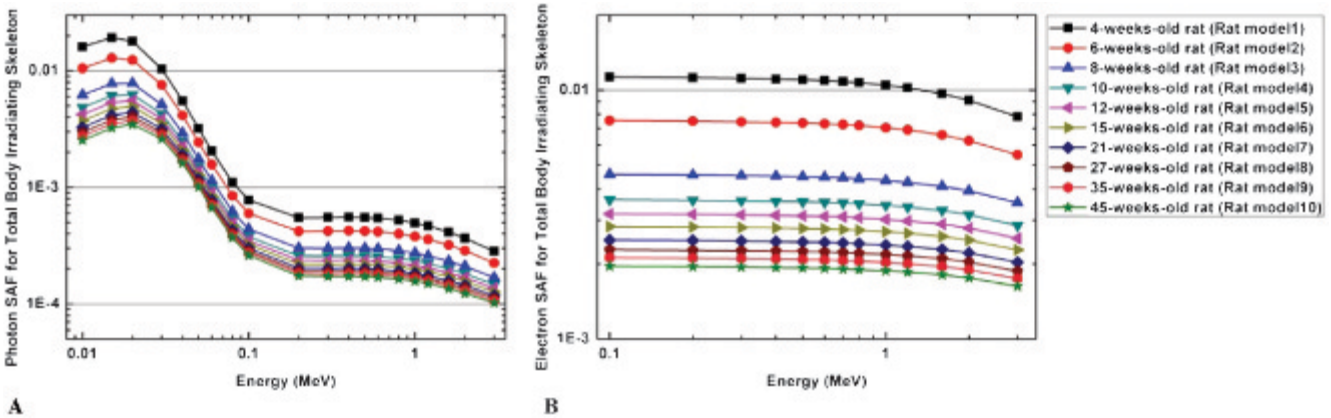

Figure 5. (A) Photon and (B) electron specific absorbed fractions (SAFs) for the total body irradiating the skeleton.

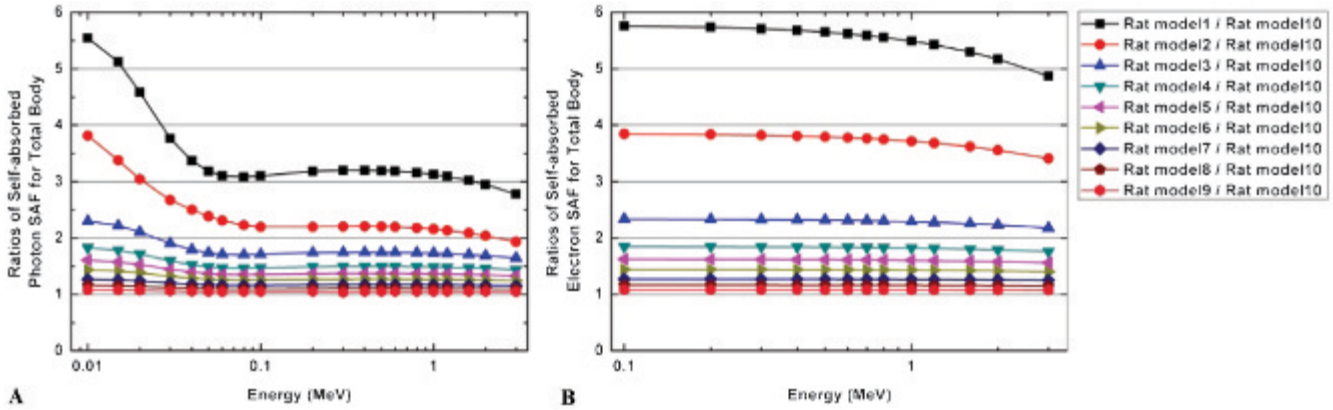

Figure 6. Ratios of self-absorbed specific absorbed fractions (SAFs) for the total body between the nine computational rat models and the oldest rat model (46 weeks) for (A) photons and (B) electrons.

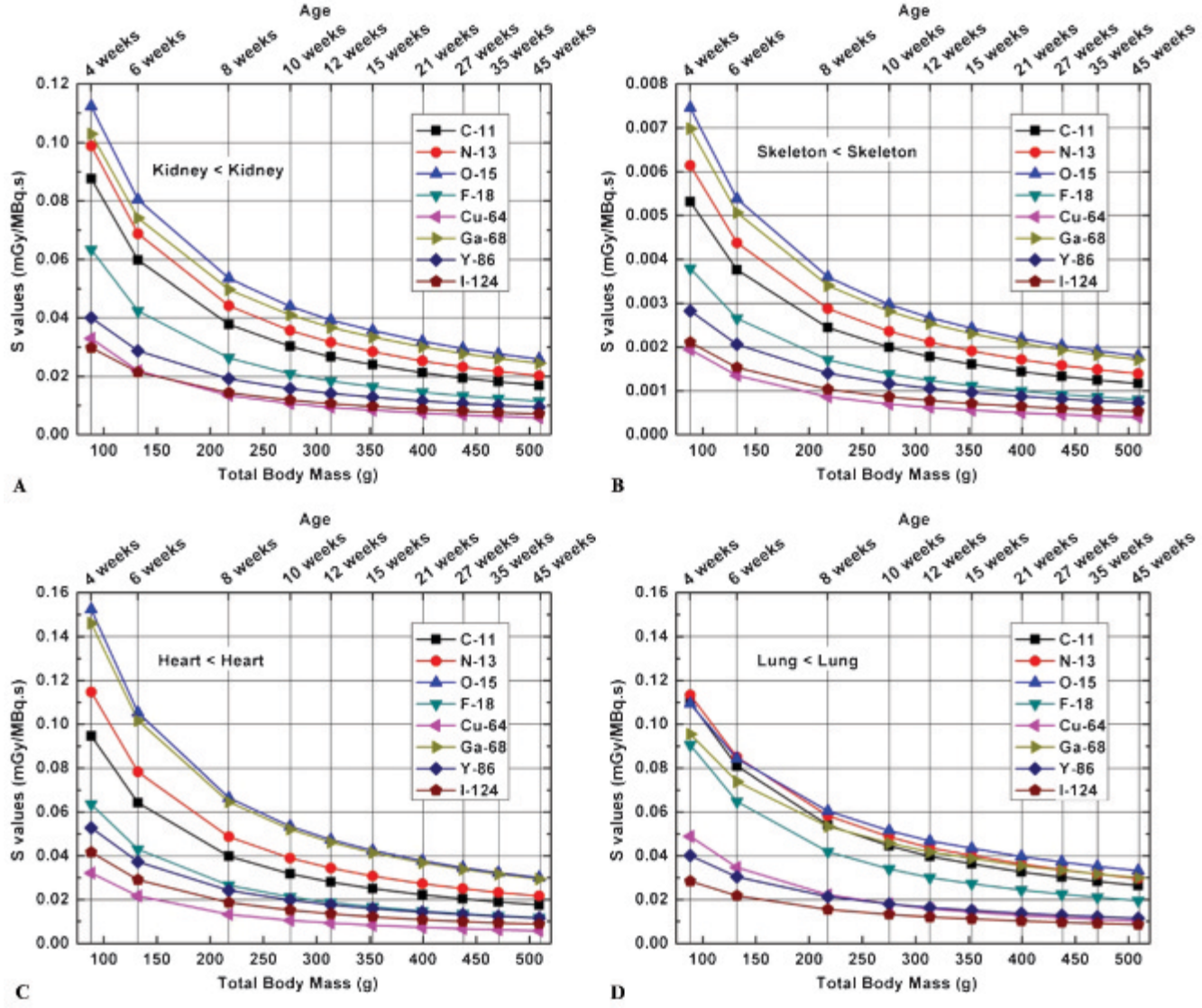

Figure 7. Representative self-absorbed S values for the (A) kidney, (B) skeleton, (C) heart, and (D) lung as a function of body mass for different positron-emitting radionuclides.

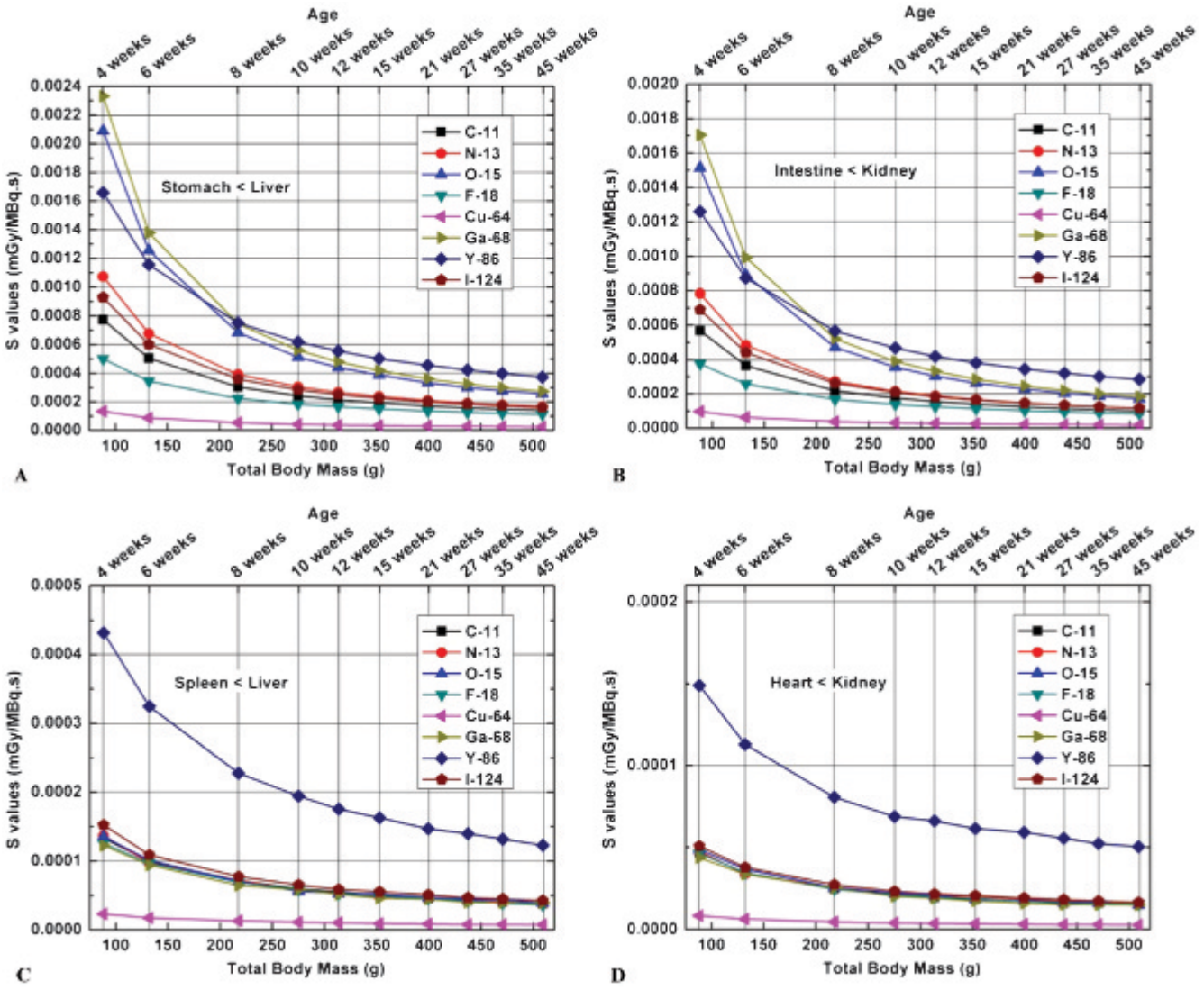

Figure 8. Representative cross-absorbed S values for (A) the liver irradiating the stomach, (B) the kidney irradiating the intestine, (C) the liver irradiating the spleen, and (D) the kidney irradiating the heart as a function of body mass for different positron-emitting radionuclides.

F-18 as an example, the difference in S values between the 4-week-old rat model to the 45-week-old rat model for most source-target pairs ranges between −1.5% and −2% per 10 g of difference in body weight.

Based on the calculated S values and biodistribution data gathered from small-animal PET studies, the absorbed doses of ^{11}C-DASB in the 10 developed anatomic rat models were calculated and compared. For all evaluated organs, the calculated absorbed dose decreases with increasing body weight. The difference between absorbed dose in these organs ranges between −1.7% and −2.1% per 10 g difference in body weight from the 4-week-old rat model to the 45-week-old rat model. The above analysis suggests that for all organs, the absorbed dose in low-weight young specimens would be considerably higher than that in adult specimens. This dose-weight/dose-age correlation is also observed in humans, where the absorbed dose per unit activity administered in pediatric patients is significantly higher than that in adult patients.[50]

Conclusion

A systematic study was performed to evaluate how dosimetric results vary with changes in age-related body weight. We investigated separately the effects of changes in small-animal weight on the calculation of AFs and SAFs of monoenergy photons/electrons and S values of positron-emitting radionuclides, as well as the organ-absorbed doses for a ^{11}C-labeled probe. For most organs in the rat body, the self-absorbed AF is positively correlated to the weight,

Table 3. Percent Difference between F-18 S Values per 10 g difference (%/10g) in Total Body Mass from the 4-Week-Old to the 45-Week-Old Rat Model

	Skeleton	*Heart*	*Lung*	*Liver*	*Stomach*	*Kidney*	*Intestines*	*Spleen*	*Bladder*	*Testis*	*Brain*	*Thyroid*	*Pancreas*	*Total Body*
Skeleton	−1.87	−1.73	−2.05	−1.77	−1.71	−1.66	−1.69	−1.69	−1.67	−1.74	−1.88	−1.66	−1.66	−1.93
Heart	−1.70	−1.94	−2.01	−1.66	−1.62	−1.57	−1.61	−1.63	−1.66	−1.76	−1.57	−1.52	−1.56	−1.92
Lung	−2.05	−2.00	−1.86	−1.94	−1.61	−1.58	−1.60	−1.59	−1.62	−1.58	−1.65	−2.11	−1.44	−1.92
Liver	−1.77	−1.66	−1.93	−1.96	−1.84	−1.88	−1.73	−1.67	−1.59	−1.63	−1.63	−1.58	−1.73	−1.92
Stomach	−1.73	−1.62	−1.60	−1.84	−1.95	−1.64	−1.77	−1.92	−1.55	−1.71	−1.64	−1.65	−1.96	−1.92
Kidney	−1.66	−1.68	−1.54	−1.87	−1.65	−1.95	−1.84	−1.69	−1.57	−1.50	−1.64	−1.55	−1.97	−1.92
Intestines	−1.69	−1.58	−1.56	−1.73	−1.77	−1.84	−1.93	−1.77	−1.84	−1.66	−1.71	−1.60	−1.87	−1.92
Spleen	−1.71	−1.57	−1.55	−1.68	−1.93	−1.69	−1.79	−1.89	−1.58	−1.61	−1.88	−1.59	−1.92	−1.92
Bladder	−1.59	−1.54	−1.61	−1.61	−1.51	−1.64	−1.82	−1.61	−1.91	−1.53	−1.91	−1.78	−1.65	−1.91
Testis	−1.78	−1.47	−0.77	−1.70	−1.84	−1.48	−1.77	−1.68	−1.52	−1.86	−2.03	0.05	−1.67	−1.92
Brain	−1.87	−1.59	−1.68	−1.58	−1.62	−1.78	−1.72	−1.63	−1.78	−1.59	−1.94	−1.67	−1.70	−1.93
Thyroid	−1.69	−1.32	−2.11	−1.54	−1.64	−1.55	−1.59	−1.64	−1.56	−2.02	−1.67	−1.91	−1.44	−1.94
Pancreas	−1.70	−1.59	−1.55	−1.74	−1.96	−1.98	−1.86	−1.93	−1.54	−1.63	−1.67	−1.73	−1.95	−1.91
Total body	−1.91	−1.90	−1.90	−1.90	−1.90	−1.89	−1.90	−1.90	−1.89	−1.91	−1.91	−1.91	−1.89	−1.91

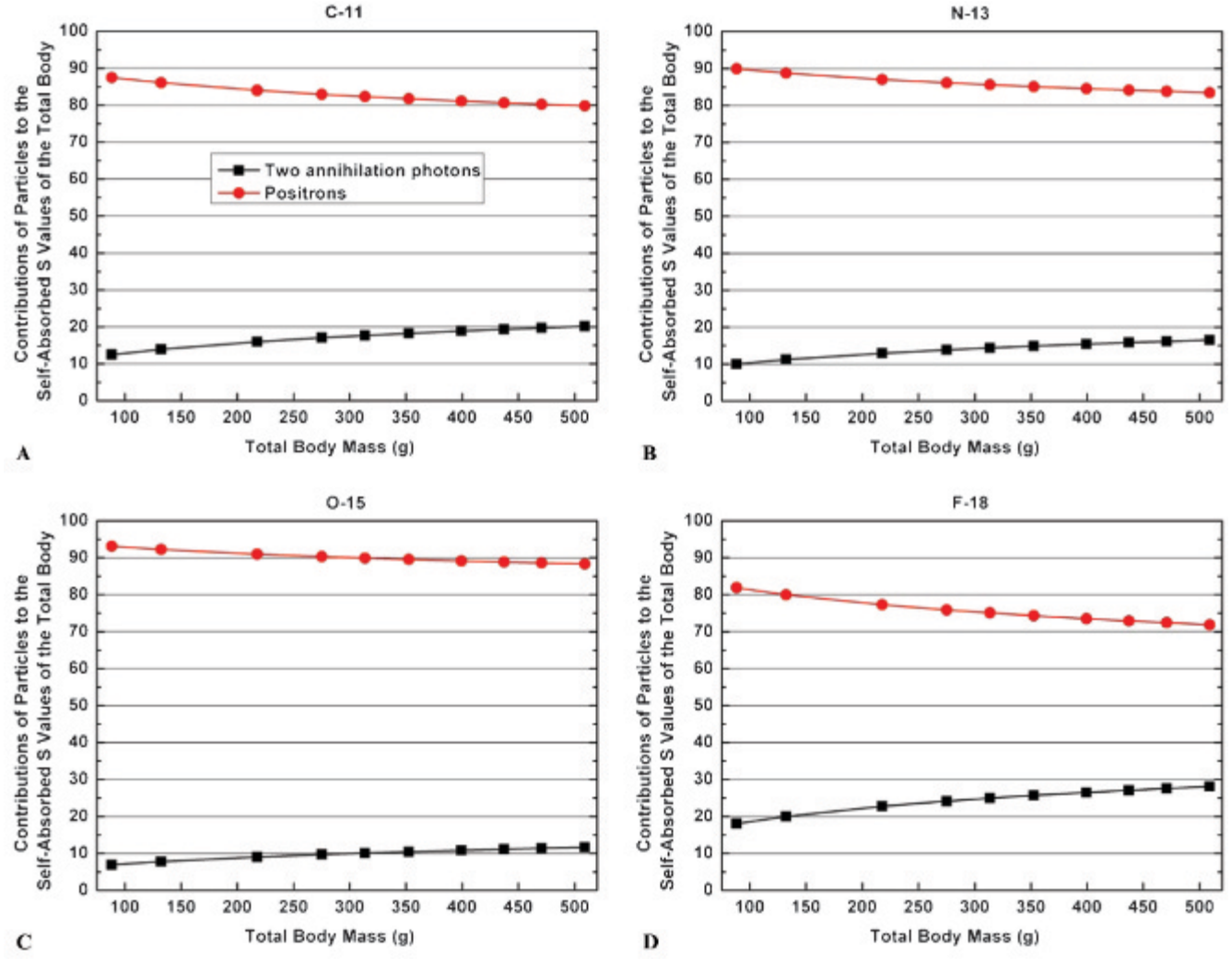

Figure 9. Proportions of contributions to self-absorbed S values of total body from positrons and the two annihilation photons for (A) C-11, (B) N-13, (C) O-15, and (D) F-18.

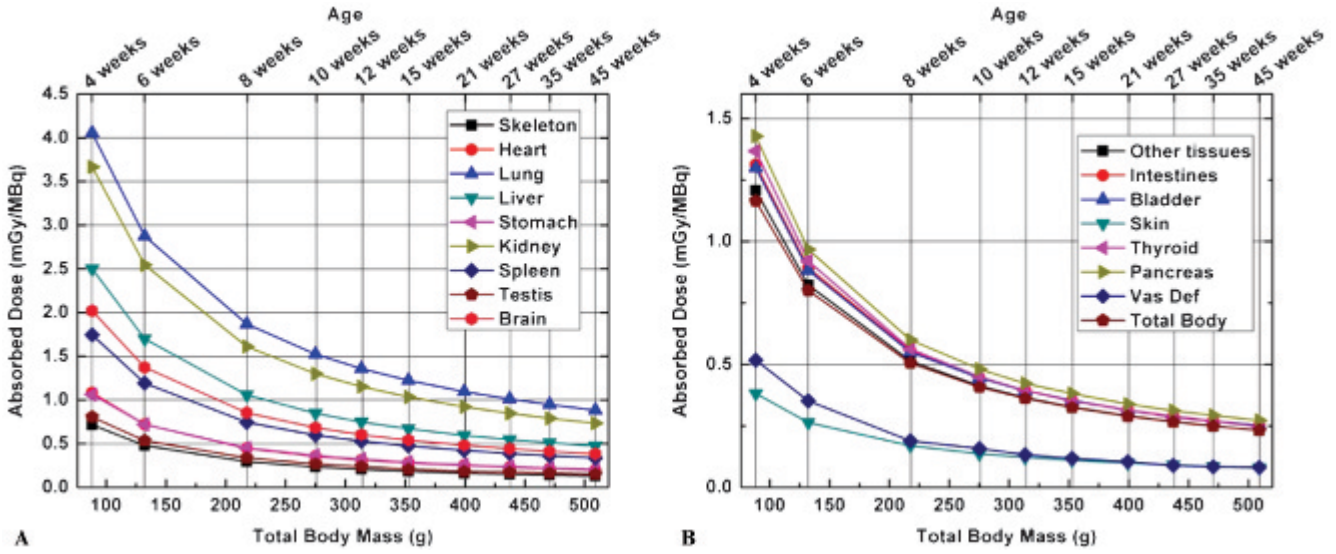

Figure 10. Absorbed doses from ^{11}C-DASB to internal organs of the 10 computational rat models at different ages.[46]

whereas the SAF and radionuclide-specific S value present an inverse correlation with body weight. In the rat body, the total S value for positron emitters is mostly contributed by positron interactions. For certain radiotracers, the absorbed dose to organs is negatively correlated with the rat body weight and would be significantly higher in low-weight young animals than in adult animals. Small-animal radiation dosimetry should be evaluated more carefully in multimodality molecular imaging experiments involving the use of young laboratory animals. The developed computational rat models can also be used for external radiation dose calculations. The produced SAFs of monoenergy photons/electrons and S values of positron-emitting radionuclides can be exploited for the assessment of radiation dose delivered by other radionuclides and various radiotracers used in small-animal trials.

Acknowledgment

Financial disclosure of authors: This work was supported by the Swiss National Science Foundation under grant SNSF 31003A-125246, the Geneva Cancer League, and the Indo-Swiss Joint Research Programme ISJRP 138866.

Financial disclosure of reviewers: None reported.

References

1. Clause BT. The Wistar rat as a right choice: establishing mammalian standards and the ideal of a standardized mammal. J Hist Biol 1993;26:329–49, doi:10.1007/BF01061973.
2. Clause BT. The Wistar Institute archives: rats (not mice) and history. Mendel Newsletter. Available at: http://www.amphilsoc.org/library/mendel/1998.htm (accessed 2012).
3. Jönsson BA, Strand SE, Larsson BS. A quantitative autoradiographic study of the heterogeneous activity distribution of different indium-111-labeled radiopharmaceuticals in rat tissues. J Nucl Med 1992;33:1825.
4. Pasqualini R, Duatti A, Bellande E, et al. Bis (dithiocarbamato) nitrido technetium-99m radiopharmaceuticals: a class of neutral myocardial imaging agents. J Nucl Med 1994;35:334.
5. Chatziioannou AF. Molecular imaging of small animals with dedicated PET tomographs. Eur J Nucl Med Mol Imaging 2002;29:98–114, doi:10.1007/s00259-001-0683-3.
6. Hui TE, Fisher DR, Kuhn JA, et al. A mouse model for calculating cross-organ beta doses from yttrium-90-labeled immunoconjugates. Cancer 1994;73(3 Suppl):951–7.
7. Konijnenberg MW, Bijster M, Krenning EP, De Jong M. A stylized computational model of the rat for organ dosimetry in support of preclinical evaluations of peptide receptor radionuclide therapy with (90)Y, (111)In, or (177)Lu. J Nucl Med 2004;45:1260–9.
8. Xie T, Zhang G, Li Y, Liu Q. Comparison of absorbed fractions of electrons and photons using three kinds of computational phantoms of rat. Appl Phys Lett 2010;97:33702–4, doi:10.1063/1.3462793.
9. Flynn AA, Green AJ, Pedley RB, et al. A mouse model for calculating the absorbed beta-particle dose from (131)I- and (90)Y-labeled immunoconjugates, including a method for dealing with heterogeneity in kidney and tumor. Radiat Res 2001;156:28–35, doi:10.1667/0033-7587(2001)156[0028:AMMFCT]2.0.CO;2.
10. Miller WH, Hartmann-Siantar C, Fisher D, et al. Evaluation of beta-absorbed fractions in a mouse model for 90Y, 188Re, 166Ho, 149Pm, 64Cu, and 177Lu radionuclides. Cancer Biother Radiopharm 2005;20:436–49, doi:10.1089/cbr.2005.20.436.
11. Hindorf C, Ljungberg M, Strand SE. Evaluation of parameters influencing S values in mouse dosimetry. J Nucl Med 2004;45:1960–5.
12. Stabin MG, Peterson TE, Holburn GE, Emmons MA. Voxel-based mouse and rat models for internal dose calculations. J Nucl Med 2006;47:655–9.
13. Kolbert KS, Watson T, Matei C, et al. Murine S factors for liver, spleen, and kidney. J Nucl Med 2003;44:784–91.

14. Bitar A, Lisbona A, Thedrez P, et al. A voxel-based mouse for internal dose calculations using Monte Carlo simulations (MCNP). Phys Med Biol 2007;52:1013–25, doi:10.1088/0031-9155/52/4/010.
15. Dogdas B, Stout D, Chatziioannou AF, Leahy RM. Digimouse: a 3D whole body mouse atlas from CT and cryosection data. Phys Med Biol 2007;52:577–87, doi:10.1088/0031-9155/52/3/003.
16. Mohammadi A, Kinase S. Monte Carlo simulations of photon specific absorbed fractions in a mouse voxel phantom. Prog Nucl Sci Technol 2011;1:126–9.
17. Zhang X, Xie X, Cheng J, et al. Organ dose conversion coefficients based on a voxel mouse model and MCNP code for external photon irradiation. Radiat Prot Dosimetry 2012;148:9–19, doi:10.1093/rpd/ncr003.
18. Peixoto PH, Vieira JW, Yoriyaz H, Lima FR. Photon and electron absorbed fractions calculated from a new tomographic rat model. Phys Med Biol 2008;53:5343–55, doi:10.1088/0031-9155/53/19/005.
19. Wu L, Zhang G, Luo Q, Liu Q. An image-based rat model for Monte Carlo organ dose calculations. Med Phys 2008;35:3759–64, doi:10.1118/1.2952647.
20. Xie T, Liu Q, Zaidi H. Evaluation of S-values and dose distributions for (90)Y, (131)I, (166)Ho, and (188)Re in seven lobes of the rat liver. Med Phys 2012;39:1462–72, doi:10.1118/1.3681009.
21. Xie T, Zaidi H. Monte Carlo-based evaluation of S-values in mouse models for positron-emitting radionuclides. Phys Med Biol 2013;58:169–82, doi:10.1088/0031-9155/58/1/169.
22. Sengupta P. A scientific review of age determination for a laboratory rat: how old is it in comparison with human age? Biomed Int 2011;2:81–9.
23. Romijn HJ, Hofman MA, Gramsbergen A. At what age is the developing cerebral cortex of the rat comparable to that of the full-term newborn human baby? Early Hum Dev 1991;26:61–7, doi:10.1016/0378-3782(91)90044-4.
24. Vidair CA. Age dependence of organophosphate and carbamate neurotoxicity in the postnatal rat: extrapolation to the human. Toxicol Appl Pharmacol 2004;196:287–302, doi:10.1016/j.taap.2003.12.016.
25. Robinson IC, Fairhall K, Hendry JH, Shalet SM. Differential radiosensitivity of hypothalamo-pituitary function in the young adult rat. J Endocrinol 2001;169:519–26, doi:10.1677/joe.0.1690519.
26. Ellis L, Baptista M. A proposed mechanism for the differential radiosensitivity of the immature rat testis. Department of Zoology, Utah State University, Logan. 1969. Available at: http://www.osti.gov/bridge/servlets/purl/4626069/4626069.pdf (accessed 2012).
27. Fukuda S, Iida H. Age difference in deposition of plutonium in organs of rats and the estimation of distribution in humans. 3rd European IRPA Congress, 2010; Helsinki, Finland, 14–18 June 2010. Available at: http://www.irpa.net/irpa10/cdrom/00464.pdf (accessed 2012).
28. Inaba J, Nishimura Y, Ichikawa R. Effect of age on the metabolism of some important radionuclides in the rat. Radiat Risk Protect 1984;1:481–4.
29. Merriam G Jr, Szechter A. The relative radiosensitivity of rat lenses as a function of age. Radiat Res 1975;62:488–97, doi:10.2307/3574142.
30. Mandl AM. The radio-sensitivity of oocytes at different stages of maturation. Proc R Soc Lond B Biol Sci 1963;158:119–41, doi:10.1098/rspb.1963.0038.
31. Segars WP, Tsui BMW, Frey EC, et al. Development of a 4-D digital mouse phantom for molecular imaging research. Mol Imaging Biol 2004;6:149–59, doi:10.1016/j.mibio.2004.03.002.
32. Keenan MA, Stabin MG, Segars WP, Fernald MJ. RADAR realistic animal model series for dose assessment. J Nucl Med 2010;51:471–6, doi:10.2967/jnumed.109.070532.
33. Pass D, Freeth G. The rat. Anzccart News 1993;6(4):1–4.
34. Global Alliance for Laboratory Animal Standardization (GALAS). Wistar Hannover GALAS growth and survival rates. Available at: http://www.galas.org/WH_data.htm2012 (accessed 2012).
35. Donaldson HH. The rat: data and reference tables for the albino rat and the Norway rat; Philadelphia, 1915; Available at http://archive.org/details/ratreferencetabl00dona (accessed 2012).
36. Xie T, Han D, Liu Y, et al. Skeletal dosimetry in a voxel-based rat phantom for internal exposures to photons and electrons. Med Phys 2010;37:2167–78, doi:10.1118/1.3380223.
37. Pelowitz D. MCNPX user's manual version 2.5.0. Los Alamos (NM): Los Alamos National Laboratory; 2005.
38. Goldstone KE. Tissue substitutes in radiation dosimetry and measurement. ICRU report 44. Vol 41. Bethesda (MD): International Commission on Radiation Units and Measurements; 1990.
39. Valentin J. Basic anatomical and physiological data for use in radiological protection: reference values. Ann ICRP 2002;32:i-265.
40. Health Physics Society. Radionuclide decay data. Available at: http://hps.org/publicinformation/radardecaydata.cfm (accessed 2012).
41. Loevinger R, Budinger T. MIRD primer for absorbed dose calculations (revised edition). Reston (VA): Society of Nuclear Medicine; 1991.
42. Bolch WE, Eckerman KF, Sgouros G, Thomas SR. MIRD pamphlet no. 21: a generalized schema for radiopharmaceutical dosimetry - standardization of nomenclature. J Nucl Med 2009;50:477–84, doi:10.2967/jnumed.108.056036.
43. Brown WD, Oakes TR, DeJesus OT, et al. Fluorine-18-fluoro-L-DOPA dosimetry with carbidopa pretreatment. J Nucl Med 1998;39:1884–91.
44. Snyder WS, Ford MR, Warner GG, Watson SB. MIRD pamphlet no. 11: 'S,' absorbed dose per unit cumulated activity for selected radionuclides and organs. New York: Society of Nuclear Medicine; 1975.
45. Bardies M, Chatal JF. Absorbed doses for internal radiotherapy from 22 beta-emitting radionuclides: beta dosimetry of small spheres. Phys Med Biol 1994;39:961–81, doi:10.1088/0031-9155/39/6/004.
46. Wilson AA, Ginovart N, Hussey D, et al. In vitro and in vivo characterisation of [11C]-DASB: a probe for in vivo measurements of the serotonin transporter by positron emission tomography. Nucl Med Biol 2002;29:509, doi:10.1016/S0969-8051(02)00316-5.
47. Sikov MR. Effect of age on the iodine-131 metabolism and the radiation sensitivity of the rat thyroid. Radiat Res 1969;38:449–59, doi:10.2307/3572786.
48. Sikov M, Mahlum D, Howard E. Effect of age on the morphologic response of the rat thyroid to irradiation by iodine-131. Radiat Res 1972;49:233–44, doi:10.2307/3573387.
49. Shimada Y, Yasukawa-Barnes J, Kim RY, et al. Age and radiation sensitivity of rat mammary clonogenic cells. Radiat Res 1994;137:118–23, doi:10.2307/3578800.
50. Mattsson S, Johansson L, Liniecki J, et al. Radiation dose to patients from radiopharmaceuticals. ICRP publication 106 (addendum 3 to ICRP publication 53). Ann ICRP 2007;38:1–197.